Thermal Multiferroics in all Inorganic Quasi-Two-Dimensional Halide Perovskites

Tong Zhu[1]†, Xue-Zeng Lu[2]†, Takuya Aoyama[3], Koji Fujita[4], Yusuke Nambu[5,6,7], Takashi Saito[8], Hiroshi Takatsu[1], Tatsushi Kawasaki[4], Takumi Terauchi[4], Shunsuke Kurosawa[5,9,10], Akihiro Yamaji[5,9], Hao-Bo Li[11,12], Cédric Tassel[1], Kenya Ohgushi[3], James M. Rondinelli[2]*, Hiroshi Kageyama[1]*

[1]Department of Energy and Hydrocarbon Chemistry, Graduate School of Engineering, Kyoto University, Nishikyo-ku, Kyoto, 615-8510, Japan.

[2]Department of Materials Science and Engineering, Northwestern University, Evanston, Illinois, 60208, USA.

[3]Department of Physics, Graduate School of Science, Tohoku University, Sendai, 980-8578, Japan.

[4]Department of Material Chemistry, Kyoto University, Nishikyo-ku, Kyoto, 615-8510, Japan.

[5]Institute for Materials Research, Tohoku University, Sendai, 980-8577, Japan.

[6]Organization for Advanced Studies, Tohoku University, Sendai, 980-8577, Japan.

[7]FOREST, Japan Science and Technology Agency, Kawaguchi, Saitama, 332-0012, Japan.

[8]Institute of Materials Structure Science, High Energy Accelerator Research Organization (KEK), Tokai, Ibaraki, 319-1106, Japan.

[9]New Industry Creation Hatchery Center (NICHe), Tohoku University, Sendai, 980-8578, Japan.

[10]Institute of Laser Engineering, Osaka University, Suita, Osaka, 990-8560, Japan.

[11]SANKEN, Osaka University, Ibaraki, Osaka, 567-0047, Japan.

[12]Spintronics Research Network Division, Institute for Open and Transdisciplinary Research Initiatives, Osaka University, Suita, Osaka, 565-0871, Japan.

*Corresponding author. Email: kage@scl.kyoto-u.ac.jp (H.K.); jrondinelli@northwestern.edu (J.M.R.)

†These authors contributed equally to this work

Introductory Paragraph

Multiferroic materials, in particular those possess simultaneous electric and magnetic order, offer a platform to design technologies and to study new physics. Despite the substantial progress and evolution of multiferroics, one priority in the field remains to be the discovery of new materials, especially those offering different mechanisms for controlling electric and magnetic orders. Here, we demonstrate simultaneous thermal control of electric and magnetic polarizations in quasi-two-dimensional halides $(K,Rb)_3Mn_2Cl_7$, arising from a polar to antipolar transition as evidenced using both X-ray and neutron powder diffraction. Our density functional theory calculations indicate a possible polarization switching path including a strong coupling between electric and magnetic order in our halide materials suggesting a magnetoelectric coupling, a situation not realised in oxide analogues. We expect our findings to stimulate the exploration of non-oxide multiferroics and magnetoelectrics to open access to alternative mechanisms, beyond conventional electric and magnetic control, for coupling ferroic orders.

Main Texts

The discovery of above-room-temperature multiferroic $BiFeO_3$[1]and spin-driven multiferroic $TbMnO_3$[1] led to the renaissance in multiferroic materials. Although the initial driver behind the research was the electric-field-control of magnetism to design non-volatile, energetically efficient magnetic storage devices[2], the progressive understanding in the field has since substantially widened the potential application of multiferroic materials[3], e.g., ranging from scalable energy-efficient magnetoelectric spin-orbit (MESO) logic[4] to magnetoelectric nanorobots for targeted drug delivery[5]. Additionally, their broken space-inversion and time-inversion symmetry is analogous and hence closely related to other fields in fundamental physics with similar symmetry requirements, such as magnetic monopoles[6] and early-universe cosmic string formation[3].

While the discovery of high temperature multiferroic materials with strong coupling remains one of the top priorities, searching for single-phase compounds exhibiting new multiferroic controlling mechanism is equivalently important, as they can open opportunities for applications and physics not considered before[7]. However, the development of new multiferroic materials is hampered by intrinsic chemical incompatibility[8]. Specifically, non-centrosymmetric, polar crystal structures needed for electric polarization are typically stabilized by second-order Jahn-Teller distortions[9] of closed-shell cations with either d^0 or ns^2 electronic configurations[8], which are incompatible with magnetic properties which require unpaired electrons. Multiple approaches have been utilized to circumvent the contra-indication. In Type-I multiferroics, polar distortions and magnetism are introduced from different cations, typically in complex oxides, e.g., $BiFeO_3$[10]. Alternative single-phase multiferroics such as rare-earth manganates rely on polar noncollinear magnetic order[1,11], which are categorized as Type-II multiferroics.

Recently, hybrid-improper ferroelectricity (HIF) has emerged as an alternative and promising mechanism to realize multiferroics with strong magnetoelectric coupling[12]. Under this mechanism, typically in quasi-2D perovskite oxides such as $A_3B_2O_7$ Ruddlesden-Popper (RP) phases, two non-polar octahedral rotations couple to a third polar distortion to give electric polarizations[13]. This mechanism has at least three advantages: First, polar structures arise from size-mismatch between cations, and there is no special electronic structure requirement. Therefore, it is tactically simpler to unify electric polarizations with long-range magnetic order. Second, both electric and magnetic polarizations are coupled to the same structural distortions, from which a strong coupling between the two ferroic orders is anticipated. Despite these merits, only very few oxide candidates have been experimentally identified, including $Ca_3Mn_2O_7$[12,14], $[Ca_{0.69}Sr_{0.46}Tb_{1.85}Fe_2O_7]_{0.85}[Ca_3Ti_2O_7]_{0.15}$[15] and $MnSrTa_2O_7$[16]. Third, the primary order parameter in HIF multiferroics is octahedral rotation, which is not only susceptible to an electric field, but other stimuli such as temperature, pressure and strain, implying that multiferroic control may be triggered by stimuli other than the conventional electric fields, although such control has not been realised in any of oxide HIF multiferroics.

Here we prepared and examined a series of the first inorganic halide HIF multiferroic materials $(K,Rb)_3Mn_2Cl_7$ with quasi-2D-perovskite structures. Employing halides rather than oxides offers a better chance to combine two ferroic orders, because the large total negative charge from oxide anions requires high valent B-site cations (typically 4+ or 5+) and this limits the number of paramagnetic (PM) cations one can choose, one main reason behind the limited amount of HIF multiferroic/magnetoelectric oxides. In contrast, divalent magnetic cations can be easily incorporated into the B-site of halide perovskites due to the lower charge of the halide anions. The presence of a large number of divalent magnetic cations suitable for octahedral geometry, together with the wide variety of nonmagnetic monovalent cations (such as alkali metals) for A-site, enable a rational design of a large family of new HIF multiferroics. Crucially, we show simultaneous thermal manipulation of the electric and magnetic polarizations in these materials. This new controlling mechanism is triggered by a thermal-induced polar-to-antipolar structural transition, which has never been observed in HIF oxide multiferroics.

Polycrystalline $K_3Mn_2Cl_7$ was synthesized via a ceramic synthesis route from KCl and $MnCl_2$, with a modified condition from a previous report[17]. Refinements against low-temperature synchrotron X-ray diffraction (SXRD) and neutron powder diffraction (NPD) data (Supplementary Information Fig. S1, Tables S1, S2) reveal it adopts a polar, $a^-a^-c^+/a^-a^-c^+$ distorted, n = 2 RP structure, in space group $A2_1am$ (Fig. 1a). This low-temperature polar structure is unambiguously demonstrated by pyroelectric and second-harmonic generation data (Fig. 1c, Supplementary Information Fig. S31). It arises from a HIF mechanism by combining a^-a^- out-of-phase rotations (X_3^- irreducible representation, irrep), c^+ in-phase rotation (X_2^+ irrep), and a polar Γ_5^- distortion through a trilinear coupling interaction $Q_{X_3^-}Q_{X_2^+}Q_{\Gamma_5^-}$ (Supplementary Information Figs. S2-S4, Table S3). On warming, $K_3Mn_2Cl_7$ undergoes a first-order transition between T_{C1} ~ 155 K and T_{C2} ~ 180 K to adopt a hybrid-improper antipolar $P4_2/mnm$ structure with $a^-b^0c^0/b^0a^-c^0$ distortion (X_3^- irrep), which stabilizes an antipolar distortion mode (M_2^+) (Supplementary Information Figs. S5-S8, Tables S4-S6). Further warming to T_A ~ 410 K leads to a transition to the undistorted $I4/mmm$ structure (Figs. 1a, 1b, Supplementary Information Figs. S9, S10, Tables S7, S8).

Zero field-cooled (ZFC) and field-cooled (FC) magnetization data (Fig. 2a) split at 64.5 K, while NPD data collected below 64.5 K (Fig. 2b) reveals a series of sharp magnetic reflections, indicating a long-range magnetic order below 64.5 K (T_N). Strong diffuse magnetic features in the NPD suggesting short-range spin correlations are observed between 64 K and 100 K, consistent with a broad maximum in magnetic susceptibility around 100 K (T_{max}). Fitting of the 4 K NPD data (Fig.

2c, Supplementary Information Fig. S11, Table S9) reveals a G-type antiferromagnetic order in magnetic space group $A2_1'am'$, with refined moments (4.36(2) μ_B) aligning along the crystallographic c-axis (Fig. 2e). This magnetic symmetry permits weak ferromagnetic (wFM) canting along the b-axis via the Dzyaloshinskii-Moriya (*DM*) interaction[18] (Fig. 2e), as evidenced by non-linear hysteretic magnetization-field isotherms (Fig. 2d) and density functional theory (DFT) calculations (Supplementary Information Figs. S17, S18, Table S11). Fitting the temperature-dependence of the ordered moments using a power law $M = M_0(1-\frac{T}{T_N})^{\beta}$ yields a Néel temperature of T_N = 64.3(1) K (Fig. 2f).

The coupling between the electric polarization and the wFM order in $K_3Mn_2Cl_7$ is established by examining the crystal and magnetic symmetries (Fig. 3a). The electric polarization (P) is directly coupled to the X_3^- out-of-phase tilt and X_2^+ in-phase rotation. The ferromagnetic order ($m\Gamma_5^+$ irrep) is established via a trilinear coupling mechanism with the X_3^- tilt and mX_1^- G-type antiferromagnetic order. Consequently, two ferroic orders are directly coupled via the X_3^- tilt, and can be simultaneously manipulated by applying an external stimulus which selectively modifies this distortion. A close inspection of the NPD data reveals a clear anomaly of the polar Γ_5^- distortion at T_N (Fig. 3b), indicating a dropping in electric polarization due to the onset of 3D magnetic order, hence a coupling effect. An anomalous negative thermal expansion (NTE) of the polar a-axis is observed below T_N, indicative of strong magnetoelastic coupling and a situation not reported in previous HIF multiferroic oxides. More direct evidences for probing magnetoelectric coupling can be obtained by future measurement of the magnetization under external fields, which likely require high-quality single crystals.

The coupling scheme established above is analogous to $Ca_3Mn_2O_7$[12], but crucially differs in switching pathways. In $Ca_3Mn_2O_7$, the lowest energy pathway to switch the polarization with the change of X_3^- rotation cannot be unambiguously established and simultaneous manipulation of polarization and magnetism has not been observed. In contrast, our calculations show the lowest energy path for $K_3Mn_2Cl_7$ involves switching the X_3^- tilt, which transforms via an antipolar intermediate $P4_2/mnm$ state (Figs. 3c, 3d). This pathway is lower in energy than transition paths through the 90° twin boundary and *Pnma* phase that have been reported in HIF RP oxides[19,20] by 4.2 meV/f.u. and 3.6 meV/f.u., respectively. To the best of our knowledge, this calculated pathway has never been unambiguously demonstrated in oxide HIF ferroelectrics/multiferroics and it is likely to also switch the wFM in $K_3Mn_2Cl_7$ (Figs. 3a, 3c, Supplementary Information Figs. S26-S29). It is important to note that the transition from $A2_1am$ to $P4_2/mnm$ must by symmetry involve a simultaneous change in directions in both local electric and magnetic polarisation (Fig. 3a).

The suggested intermediate $P4_2/mnm$ phase in the polarization switching path identified from our DFT calculations is in excellent agreements with the observed thermal phase transitions (Fig. 1a): the antipolar $P4_2/mnm$ structure is the intermediate phase. This temperature-induced polar-antipolar transition has never been realized in oxide HIF multiferroics. Given such transition involves the loss of the c^+ rotation (which does not affect ferromagnetism) and a change in the X_3^- tilt direction from a^-a^- (X_3^- (a;0)) to a^-b^0 (X_3^- (a;a)), we anticipate control of ferromagnetism (Fig. 3a, Supplementary Information Fig. S29). However, the polar-antipolar transition temperature (T_C) for $K_3Mn_2Cl_7$ is higher than the magnetic ordering temperature T_N, hence dipolar control of the magnetism cannot be directly realized in this composition. Substituting K^+ with the larger Rb^+ cation reduces the size-mismatch with manganese and stabilizes the antipolar $P4_2/mnm$ structure, lowering T_C while keeping T_N almost unchanged (Supplementary Information Figs. S22, S30). Consequently, T_C can be chemically tuned below T_N by varying Rb concentration. Large concentrations even stabilize the antipolar $P4_2/mnm$ as the ground-state structure, e.g., $K_2RbMn_2Cl_7$ adopts an antipolar $P4_2/mnm$ structure at 5 K (Supplementary Information Figs. S12-

S14, Table S10). The 5 K NPD data also reveals a similar G-type antiferromagnetic order along the *c*-axis in magnetic space group *Pnn'm'* in $K_2RbMn_2Cl_7$. The a^-b^0 tilt (X_3^- irrep) creates additional canted moments in the *ab* plane due to *DM* interactions, evidenced by non-linear, hysteretic magnetization-isotherms (Supplementary Information Figs. S15, S16). For lower Rb concentrations, such as $K_{2.85}Rb_{0.15}Mn_2Cl_7$, we find upon cooling below T_N (~ 65 K) that a structural transition from the antipolar $P4_2/mnm$ to polar $A2_1am$ occurs, accompanied by a spin-structure transition from $A2_1'am'$ to *Pnn'm'* (Fig. 4a), evidenced by SXRD, magnetic and NPD data (Fig. 4b, Supplementary Information Figs. S19-S25). During this process both electric polarization and weak-ferromagnetic moments are reorientated in quasi-2D layers. Therefore, thermally induced simultaneous manipulation of ferromagnetism and polarization through a change in the octahedral tilts is achieved in a single phase (Supplementary Information Figs. S26-S29). Such tilt-enabled multiferroic coupling has long been sought but never realized. We expect a similar effect over a wide composition range in $K_{3-x}Rb_xMn_2Cl_7$ solid-solutions when the polar-antipolar transition occurs below T_N (Fig. 4c, Supplementary Information Fig. S30).

For decades, research in multiferroics and magnetoelectrics has focused on using electric or magnetic field to control ferroic orders. We have shown that the concept can be thermally accessible in the first halide-based HIF multiferroics. The thermal induced simultaneous reorientations (but not switching) of electric and ferromagnetic polarizations are achieved directly using thermal energy without thermomechanical mediation. Such unusual control is enabled by the evolution of octahedral rotation from a^-a^- to a^-b^0, which has not been identified in oxide HIF multiferroics. The distinct anion chemistry is perhaps behind the different phase transition behaviours and switching paths between oxides and chlorides, which require further experimental and theoretical evidences for verification. Although the transition in our current materials is polar-antipolar, there is no reason to expect that thermal multiferroic materials with polar-polar structural transition cannot be designed.

In addition to our HIF multiferroic halides, there exist other 2D and quasi-2D multiferroic halides enabled by different mechanisms. Typical examples include 2D van der Waals (vdW) multiferroics such as transition metal dihalides[21], and the improper BaMF$_4$ family (M = Mn/Ni/Co/Fe/Cu)[22]. Despite their chemical similarities with our materials, their underlying multiferroic mechanisms and potential switching paths are different. Specifically, 2D vdW multiferroics, such as NiI_2, are type-II multiferroics and reply on a non-centrosymmetric spin texture to induce its electric polarisation[21]. BaMF$_4$ are conceptually more similar to our materials as they also belong to improper geometric ferroelectrics. However, they melt before undergoing a ferroelectric transition and hence the switching path remains ambiguous[22].

Is similar dipolar thermal control possible in other multiferroic materials such as aforementioned non-HIF multiferroic halides? In this regard, type-II multiferroics are promising candidates, as there is no reason to prevent them from exhibiting transitions between two non-centrosymmetric spin arrangements with both electric and (weak)ferromagnetic polarisation pointing along different directions. However, low magnetic ordering temperatures may be an intrinsic challenge and such thermal control may only exist at very low temperatures. In contrast, BaMF$_4$ are unlikely to offer similar thermal control, as no polar-polar or polar-antipolar transition has been experimentally identified in this family.

The temperature-induced dipolar manipulation can be easily achieved remotely, which is appealing for *in vivo* application such as drug deliveries[3], and can be triggered by using 'side effects' such as intentional Joule heating. In addition, inducing a temperature difference is generally easier than applying a large electric or magnetic field which is normally required in controlling current multiferroics. Since structural transitions are sensitive to many external conditions such as pressure[23] and radiation[24], these stimuli are expected to achieve similar control. Besides, the fact that both polar and magnetic transition temperatures in our materials can be tuned below the nitrogen boiling point suggests that they may be studied as multicaloric materials[25,26] for ultra-low temperature refrigeration required for quantum information technologies[27].

Other halide materials with different transition metals, and/or with halide species other than chloride should be attempted and different transition metals can result in different magnetic symmetries and hence distinct coupling mechanisms. Although the magnetic ordering temperatures of layered halide perovskites (Table S12) are generally below ambient temperature, they may be elevated by chemical and structural modifications, e.g., alloying halides with oxide to strengthen the superexchange interaction in oxyhalides, or making 3D halide heterostructures, similar to the oxide $[(YFeO_3)_4(LaFeO_3)_5]_{40}$[28], to exploit 3D magnetic exchange paths that facilitate higher ordering temperatures. Finally, it would be very attractive to explore the possibility of realising thermal multiferroic systems with polar-polar structural transitions. Such systems would allow for more multiferroic states through combined electric and thermal control (Figs. S32 and S33).

Acknowledgments: The authors thank A. Kaminaka from Tohoku University for sample preparation, S. Kawaguchi and S. Kobayashi from SPring-8, JASRI for the assistance in collecting SXRD data (2020A0822). NPD experiments were performed at J-Parc BL09 SPICA beamline (2019S10) and JRR-3 HERMES beamline (22602). T. Z. acknowledges Sumitomo Chemical. H. K. and T. Z. acknowledges JSPS Core-to-Core Program (JPJSCCA202200004), JSPS Grant-in-Aid for Specially Promoted Research “Hydrogen Ion Ceramics” (JP22H04914), and JSPS Grantsin-Aid for Scientific Research (22H04914, 22H0514). T. Z. and S. K. acknowledges GIMRT Program of the Institute for Materials Research, Tohoku University (202109-RDKGE-0104). X.-Z. L. and J. M. R. were supported by the National Science Foundation under award number DMR-2011208. Computational efforts were supported by the National Energy Research Scientific Computing Center (NERSC), a U.S. DOE Office of Science User Facility located at Lawrence Berkeley National Laboratory, operated under Contract No. DE-AC02-05CH11231, and the Extreme Science and Engineering Discovery Environment (XSEDE), which is supported by NSF (ACI-1548562). T. A. was supported by the JSPS KAKENHI (20K14396). K. F. was supported by the JSPS KAKENHI (JP20K20546 and JP22H01775), the Kazuchika Okura Memorial Foundation, the Nippon Sheet Glass Foundation for Materials Science and Engineering, and the Mitsubishi Foundation.

Author contributions: T. Z., X.-Z. L., J. M. R., and H. K. designed the project. T. Z., S. K. and A. Y. synthesized samples. X.-Z. L. performed theoretical calculations. T. Z., Y. N., T. S. and C. T. collected SXRD and NPD data. T. Z. performed structural analysis, with comments from Y. N., K. F. and X.-Z. L. T. A. and K. O. performed physical property measurements. K. F., T. K. and T. T. performed SHG measurements. T. Z., H. T. and H. L. collected and analyzed magnetization data. T. Z., X.-Z. L., J. M. R., and H. K. wrote the manuscript, with comments from other authors.

Competing interests: The authors declare that they have no competing interests.

Figure Legends

Fig. 1. Structure evolution of $K_3Mn_2Cl_7$. (**a**) Schematic of tilting distortions adopted by $K_3Mn_2Cl_7$ with temperature. (**b**) Normalized lattice parameters with temperature. (**c**) Temperature-dependent dielectric constants, pyroelectric currents and electric polarizations on a polycrystalline pellet.

Fig. 2. Magnetic properties of $K_3Mn_2Cl_7$. (**a**) ZFC/FC data collected between 2 K and 300 K. (**b**) NPD data collected between 4 K and 100 K. Arrows indicate selected magnetic reflections. The bottom figure shows the expanded region from 4.5 Å to 7.5 Å where the most intense magnetic peaks appear. (**c**) Refinement of $A2_1am$ crystal and $A2_1'am'$ magnetic models against 4 K NPD data. (**d**) $M(H)$ data collected at 5 K (blue) and 70 K (red). The inserted plot is the expanded region around the origin, which clearly shows the hysteresis loop. (**e**) G-type antiferromagnetic order observed from NPD data (left) and final canted-antiferromagnetic structure (right) due to the *DM* interaction. (**f**) Power law fitting to ordered Mn moments against temperature. The ordered moments and corresponding error bars come from fitting intensities of magnetic reflections from NPD data.

Fig. 3. Symmetry relationship and indirect evidence for magnetoelectric coupling in $K_3Mn_2Cl_7$. (**a**) Magnetoelectric (ME) coupling mechanism in the polar $A2_1am$ phase and symmetry relationship in the antipolar $P4_2/mnm$ state. Switching the X_3^- (a,0) distortion switches both the electric polarization P (Γ_5^-) and weak ferromagnetism ($m\Gamma_5^+$) in the polar $A2_1am$ phase. Combining the mX_1^-antiferromagnetic order with X_3^- (a,0) (in $A2_1am$ symmetry) and X_3^- (a,a) (in $P4_2/mnm$ symmetry) leads to different weak ferromagnetic orders. (**b**) Indirect evidence for ME coupling. Top, middle, and bottom figures show magnetization, refined polar Γ_5^- distortion and polar *a*-axis against temperature. Polar Γ_5^- distortions and cell parameters along *a*-axis, as well as their corresponding error bars are obtained from fitting the variable-temperature NPD data. (**c**) Polarization energy switching barriers between $+\boldsymbol{P}$ state (left) and $-\boldsymbol{P}$ state (right) through the intermediate phase for different paths. (**d**) Mode amplitude and symmetry evolution in the polarization switching path via $P4_2/mnm$ intermediate state.

Fig. 4. Simultaneous thermal manipulation of P and M in $K_{3-x}Rb_xMn_2Cl_7$. (**a**) Illustration of thermal changes in the directions of P and M. Arrows in the top panel indicate the local electric polarizations. Arrows in the bottom panel indicate directions of wFM. Note that wFM shown above T_C in this figure represents one of several possible scenarios, which are detailed in Supporting Information Section 8. (**b**) Temperature evolution of 004 reflections (SXRD) and phase fractions from $A2_1am$ and $P4_2/mnm$ phases of $K_{2.85}Rb_{0.15}Mn_2Cl_7$. Upon cooling, there is a transition from the antipolar to polar state. (**c**) A proposed phase diagram as a function of composition and temperature. The right-hand-side figure shows an expanded region around the origin. The dashed line indicates $K_{2.85}Rb_{0.15}Mn_2Cl_7$. Circles represent experimentally observed phase transition temperatures.

Reference

1. Wang, J. *et al.* Epitaxial $BiFeO_3$ Multiferroic Thin Film Heterostructures. *Science (1979)* **299**, 1719–1722 (2003).
2. Kimura, T. *et al.* Magnetic Control of Ferroelectric Polarization. *Nature* **426**, 55–58 (2003).
3. Bibes, M. & Barthélémy, A. Towards a Magnetoelectric memory. *Nat Mater* **7**, 425–426 (2008).
4. Spaldin, N. A. Multiferroics beyond Electric-field Control of Magnetism. *Proc R Soc A: Math, Phys Eng Sci* **476**, 20190542 (2020).
5. Manipatruni, S. *et al.* Scalable Energy-efficient Magnetoelectric Spin–orbit logic. *Nature* **565**, 35–42 (2019).
6. Chen, X.-Z. *et al.* Hybrid Magnetoelectric Nanowires for Nanorobotic Applications: Fabrication, Magnetoelectric Coupling, and Magnetically Assisted In Vitro Targeted Drug Delivery. *Adv Mater* **29**, 1605458 (2017).
7. Meier, Q. N. *et al.* Search for the Magnetic Monopole at a Magnetoelectric Surface. *Phys Rev X* **9**, 11011 (2019).
8. Ponet, L. *et al.* Topologically Protected Magnetoelectric Switching in a Multiferroic. *Nature* **607**, 81–85 (2022).
9. Hill, N. A. Why Are There so Few Magnetic Ferroelectrics? *J Phys Chem B* **104**, 6694–6709 (2000).
10. Pearson, R. G. The second-order Jahn-Teller effect. *J Mol Struct: THEOCHEM* **103**, 25–34 (1983).
11. Hur, N. *et al.* Electric Polarization Reversal and Memory in a Multiferroic Material Induced by Magnetic Fields. *Nature* **429**, 392–395 (2004).
12. Benedek, N. A. & Fennie, C. J. Hybrid Improper Ferroelectricity: A Mechanism for Controllable Polarization-Magnetization Coupling. *Phys Rev Lett* **106**, 107204 (2011).
13. Yoshida, S. *et al.* Hybrid Improper Ferroelectricity in $(Sr,Ca)_3Sn_2O_7$ and Beyond: Universal Relationship between Ferroelectric Transition Temperature and Tolerance Factor in n = 2 Ruddlesden–Popper Phases. *J Am Chem Soc* **140**, 15690–15700 (2018).
14. Liu, M. *et al.* Direct Observation of Ferroelectricity in $Ca_3Mn_2O_7$ and its Prominent Light Absorption. *Appl Phys Lett* **113**, 22902 (2018).
15. J., P. M. *et al.* Tilt Engineering of Spontaneous Polarization and Magnetization above 300 K in a Bulk Layered Perovskite. *Science (1979)* **347**, 420–424 (2015).
16. Zhu, T. *et al.* Directed Synthesis of a Hybrid Improper Magnetoelectric Multiferroic material. *Nat Commun* **12**, 4945 (2021).
17. Horowitz, A., Gazit, D. & Makovsky, J. The growth of $K_3Mn_2Cl_7$, K_4MnCl_6 and $CsMn_4Cl_9$ from non-stoichiometric melts. *J Cryst Growth* **51**, 489–492 (1981).
18. Moriya, T. Anisotropic Superexchange Interaction and Weak Ferromagnetism. *Phy Rev* **120**, 91–98 (1960).
19. Nowadnick, E. A. & Fennie, C. J. Domains and Ferroelectric Switching Pathways in $Ca_3Ti_2O_7$ from First Principles. *Phys Rev B* **94**, 104105 (2016).
20. Li, S. & Birol, T. Suppressing the Ferroelectric Switching Barrier in Hybrid Improper Ferroelectrics. *NPJ Comput Mater* **6**, 168 (2020).
21. Song, Q. *et al.* Evidence for a Single-layer van der Waals Multiferroic. *Nature* **602**, 601–605 (2022).
22. Scott, J. F. & Blinc, R. Multiferroic Magnetoelectric Fluorides: Why are There so Many Magnetic Ferroelectrics? *J Phys: Condens Matter* **23**, 113202 (2011).
23. Ye, F. *et al.* Soft Antiphase Tilt of Oxygen Octahedra in the Hybrid Improper Multiferroic $Ca_3Mn_{1.9}Ti_{0.1}O_7$. *Phys Rev B* **97**, 41112 (2018).
24. Cavalleri, A. *et al.* Femtosecond Structural Dynamics in VO_2 during an Ultrafast Solid-Solid Phase Transition. *Phys Rev Lett* **87**, 237401 (2001).
25. Moya, X., Kar-Narayan, S. & Mathur, N. D. Caloric Materials near Ferroic Phase Transitions. *Nat Mater* **13**, 439–450 (2014).
26. Hou, H., Qian, S. & Takeuchi, I. Materials, Physics and Systems for Multicaloric Cooling. *Nat Rev Mater* **7**, 633–652 (2022).
27. Ladd, T. D. *et al.* Quantum Computers. *Nature* **464**, 45–53 (2010).
28. Alaria, J. *et al.* Engineered Spatial Inversion Symmetry Breaking in an Oxide Heterostructure Built from Isosymmetric Room-temperature Magnetically Ordered Components. *Chem Sci* **5**, 1599–1610 (2014).

Methods

Synthesis

Polycrystalline samples of $K_{3-x}Rb_xMn_2Cl_7$ ($0 \leq x \leq 1$) were prepared by reacting suitable stoichiometric ratios of anhydrous KCl (99.0%), RbCl (99.8%) and $MnCl_2$ (99.999%). The mixture was ground in an agate pestle and mortar in a nitrogen-filled glovebox, pelletized and loaded in a Pyrex tube. The Pyrex tube was then evacuated, sealed and heated to 410 °C at a rate of 100 °C/h and kept at 410 °C for 48 h. Samples were then transferred into the glovebox, reground, pelletized and heated in an evacuated Pyrex tube at 410 °C for another 48 h. Sample purity and reaction progress were monitored by X-ray powder diffraction data, which were collected using a Rigaku SmartLab SE diffractometer (Cu Kα radiation). Samples were kept in the glovebox to avoid exposure to air or moisture.

Structural Characterization

High-resolution synchrotron X-ray powder diffraction data were collected using instrument BL02B2 at SPring-8. Samples were packed and sealed in 0.5 mm diameter borosilicate glass capillaries. Diffraction patterns were measured using CeO_2-calibrated X-ray radiations with an approximate wavelength of 0.42 Å. Diffraction data were collected as a function of temperatures using a N_2 gas flow device ($100 \leq T/\mathrm{K} \leq 500$) and Helium gas flow temperature control device ($30 \leq T/\mathrm{K} \leq 100$). Variable-temperature neutron powder diffraction data were collected using SPICA instrument (Time-Of-Flight, TOF) at J-Parc facility and HERMES diffractometer (Constant Wavelength, CW) at Japan Research Reactor-3 (JRR-3). Rietveld profile refinements were performed using the GSAS[29], GSAS2[30] and FullProf[31] suites of programs. Symmetry and distortion mode analyses was performed using the ISODISTORT software[32].

Magnetic Measurements

Magnetization data were collected using a Quantum Design MPMS-XL SQUID magnetometry. Zero-field cooled (ZFC) and field cooled (FC) data were collected in an applied field of 0.01 T. Magnetization-field isotherms were collected with applied fields in the range $-5 \leq H/\mathrm{T} \leq 5$.

Dielectric and pyroelectric Measurements

For the measurements of dielectric constant (ε') and electric polarization (P), a sintered polycrystalline sample was pressed into thin plates and, subsequently, a gold electrode was deposited by a sputtering method on a pair of the widest surfaces. The ε' was measured at an excitation frequency of 100 kHz in a commercial ^{4}He cryostat using an LCR meter (Agilent E4980). Electric polarization was obtained by integrating a pyroelectric current measured with an electrometer (Keithley 6517).

Optical Second Harmonic Generation (SHG) Measurements

For the purpose of investigating the noncentrosymmetric nature of $K_3Mn_2O_7$, optical SHG was measured at 10 K in reflection geometry using a 1064-nm fundamental beam of a Nd:YAG laser (EKSPLA PL2143) operating with 25 ps pulses at a repetition frequency of 10 Hz. The SHG light from the polycrystalline sample was detected with a photomultiplier tube through a 532-nm narrow band-pass filter. The sample was mounted in a closed-cycle helium refrigerator.

Computational Details

Our total energy calculations are based on density functional theory (DFT) within the generalized gradient approximation (GGA) utilizing the revised Perdew-Becke-Erzenhof functional for solids (PBEsol)[33] implemented in the Vienna Ab Initio Simulation Package (VASP)[34]. We use a 550-eV plane wave cutoff energy for all calculations and the projector augmented wave (PAW) method[35]. We also use a 5×5×2 *k*-point mesh and Gaussian smearing (0.10 eV width) for the Brillouin-zone integrations. The electric polarization is computed based on linear response theory using Born effective charges and small ionic displacements with respect to a centrosymmetric reference structure[36], which is consistent with that computed by the Berry phase method[37]. We obtained converged results using an increased planewave cutoff energy of 700 eV in the calculations for the Born effective charges. We used the DFT plus Hubbard *U* method[38] with *U* and exchange parameter *J* set to 6 and 1 eV for Mn, respectively. These parameters reproduced the experimentally G-type antiferromagnetic structure. Spin-orbital coupling (SOC) is included in the magnetic anisotropy studies and the *J* value is increased to 1.5 eV to reproduce the experimentally determined magnetic anisotropy.

To compute the symmetric spin exchange parameters, the four-state mapping method is used[39]. In this study, we calculate the effective symmetric spin exchange parameters, which are obtained by setting $|S_i| = 1$, namely, $J_{ij}=J_{ij}^{eff}S_iS_j$ for a spin dimer *ij*.

Our parallel tempering Monte Carlo (PTMC) simulations are based on an exchange MC method[40], which can simulate the classical Heisenberg spin system with a Hamiltonian of $E = E_0 + \sum_{\langle i,j \rangle} J_{ij}\mathbf{S}_i \cdot \mathbf{S}_j$ where J_{ij} is the symmetric spin exchange parameter. To obtain the plot of the specific heat (*C*) versus temperature (*T*), we calculate the specific heat $C\sim(\langle E^2\rangle - \langle E\rangle^2)/T^2$ after the system reaches equilibrium at a given temperature *T* in the simulation. Then the critical temperature can be obtained by locating the peak position in the $C(\mathrm{T})$ plot. In our PTMC simulations of the effective Hamiltonian, a 6×6×3 supercell of the 48-atom unit cell is adopted for the $K_3Mn_2Cl_7$ compound, which is converged and only leads to changes of 2 K compared to a larger 12×12×2 supercell. The number of replicas is set to 96.

Data availability: Data needed to evaluate the conclusions of this paper are present in the paper and the Supplemental Materials. Additional data are available upon request from the corresponding authors.

Methods-only references

29. Larson, A. C. & von Dreele, R. B. General Structure Analysis System (GSAS)(Report LAUR 86-748). *Los Alamos, New Mexico: Los Alamos National Laboratory* (2004).
30. Toby, B. H. & von Dreele, R. B. *GSAS-II*: the Genesis of a Modern Open-source all Purpose Crystallography Software Package. *J Appl Crystallogr* **46**, 544–549 (2013).
31. Rodríguez-Carvajal, J. Recent Advances in Magnetic Structure Determination by Neutron Powder Diffraction. *Phys B Condens Matter* **192**, 55–69 (1993).
32. Campbell, B. J., Stokes, H. T., Tanner, D. E. & Hatch, D. M. '"ISODISPLACE"': a Web-based Tool for Exploring Structural Distortions. *J Appl Crystallogr* **39**, 607–614 (2006).
33. Perdew, J. P. *et al.* Restoring the Density-Gradient Expansion for Exchange in Solids and Surfaces. *Phys Rev Lett* **100**, 136406 (2008).
34. Kresse, G. & Furthmüller, J. Efficient Iterative Schemes for ab initio Total-energy Calculations using a Plane-wave Basis Set. *Phys Rev B* **54**, 11169–11186 (1996).
35. Blöchl, P. E. Projector Augmented-wave Method. *Phys Rev B* **50**, 17953–17979 (1994).
36. Meyer, B. & Vanderbilt, D. Ab initio Study of Ferroelectric Domain Walls in $PbTiO_3$. *Phys Rev B* **65**, 104111 (2002).
37. King-Smith, R. D. & Vanderbilt, D. Theory of Polarization of Crystalline Solids. *Phys Rev B* **47**, 1651–1654 (1993).
38. Liechtenstein, A. I., Anisimov, V. I. & Zaanen, J. Density-functional Theory and Strong Interactions: Orbital Ordering in Mott-Hubbard Insulators. *Phys Rev B* **52**, R5467–R5470 (1995).
39. Xiang, H. J., Kan, E. J., Wei, S.-H., Whangbo, M.-H. & Gong, X. G. Predicting the Spin-lattice Order of Frustrated Systems from First Principles. *Phys Rev B* **84**, 224429 (2011).
40. Hukushima, K. & Nemoto, K. Exchange Monte Carlo Method and Application to Spin Glass Simulations. *J Phys Soc Jpn* **65**, 1604–1608 (1996).

Supplementary information is available for this paper.

Correspondence and requests for materials should be addressed to James M. Rondinelli and Hiroshi Kageyama.

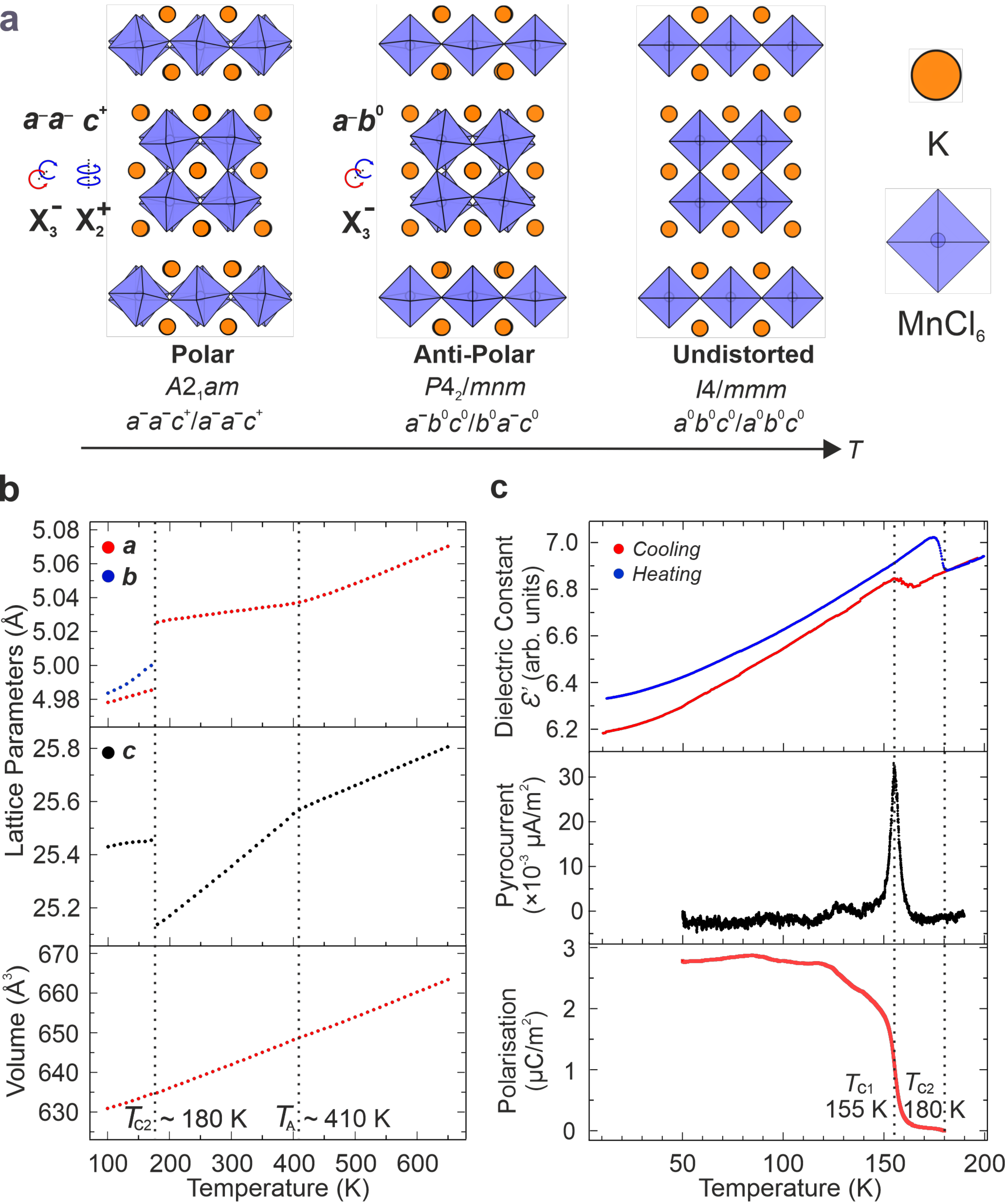

a
a⁻a⁻ c⁺
X3⁻ X2⁺
a⁻b⁰
X3⁻
K
MnCl6
Polar
A2₁am
a⁻a⁻c⁺/a⁻a⁻c⁺
Anti-Polar
P4₂/mnm
a⁻b⁰c⁰/b⁰a⁻c⁰
Undistorted
I4/mmm
a⁰b⁰c⁰/a⁰b⁰c⁰
T
b
a
b
c
Lattice Parameters (Å)
Volume (Å³)
TC2 ~ 180 K
TA ~ 410 K
Temperature (K)
c
Cooling
Heating
Dielectric Constant
ε' (arb. units)
Pyrocurrent
(×10⁻³ μA/m²)
Polarisation
(μC/m²)
TC1
155 K
TC2
180 K
Temperature (K)

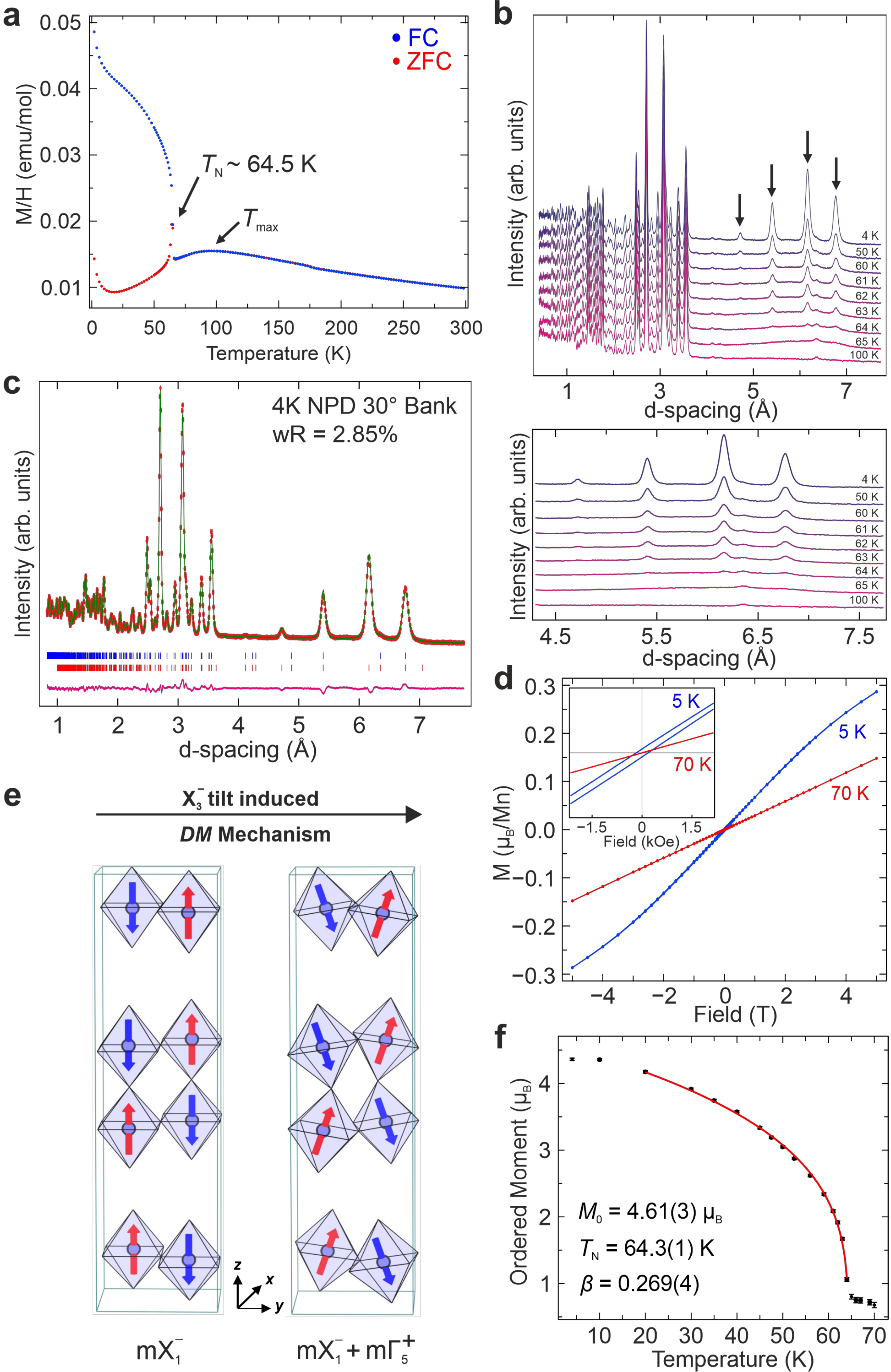

a
FC
ZFC
T_N ~ 64.5 K
T_{max}
M/H (emu/mol)
Temperature (K)
b
Intensity (arb. units)
d-spacing (Å)
4 K
50 K
60 K
61 K
62 K
63 K
64 K
65 K
100 K
c
4K NPD 30° Bank
wR = 2.85%
Intensity (arb. units)
d-spacing (Å)
d
5 K
70 K
Field (kOe)
M (μ_B/Mn)
Field (T)
e
X_3^- tilt induced
DM Mechanism
mX_1^-
$mX_1^- + m\Gamma_5^+$
f
M_0 = 4.61(3) μ_B
T_N = 64.3(1) K
β = 0.269(4)
Ordered Moment (μ_B)
Temperature (K)

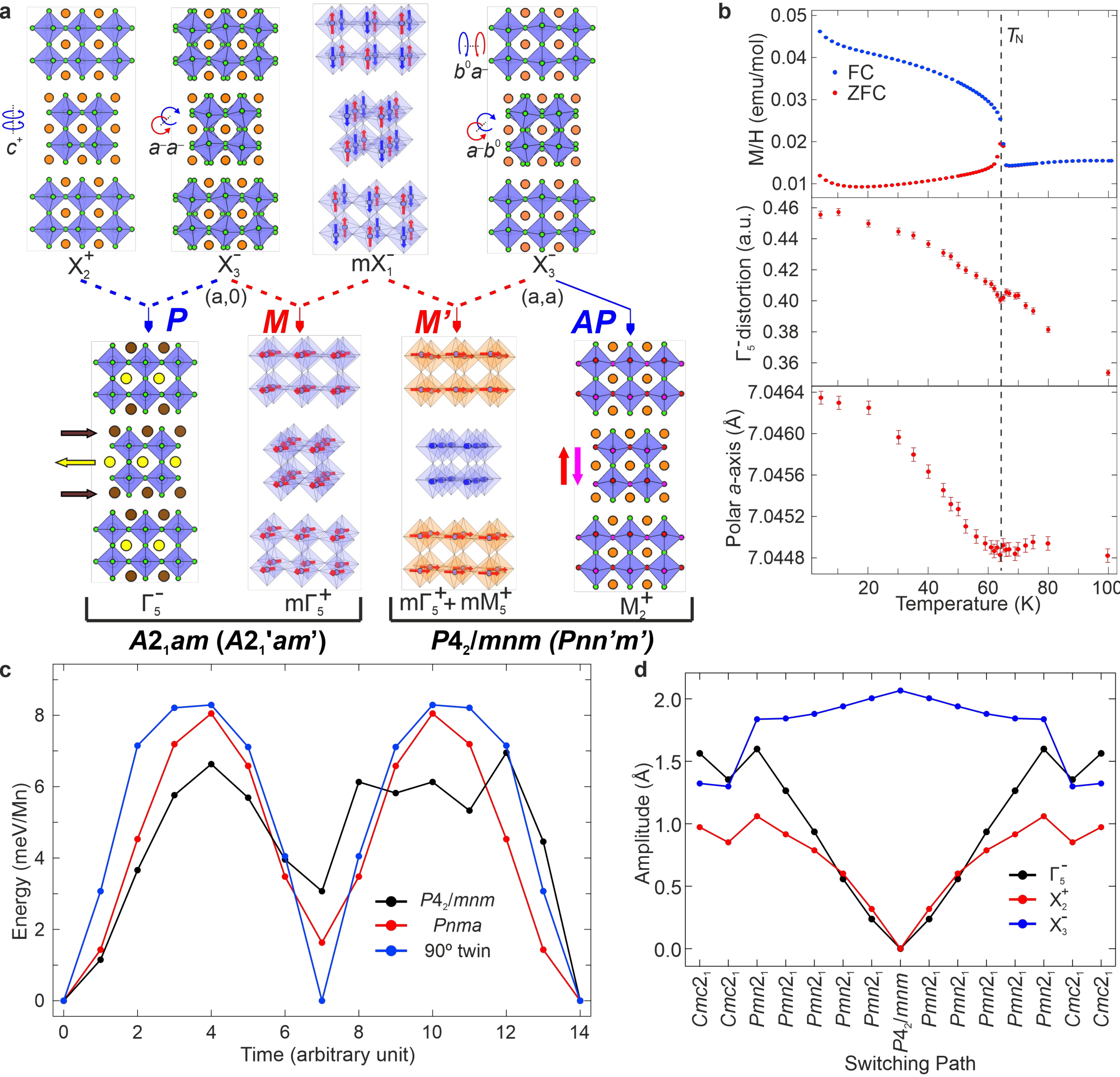

a
c+
a-a-
b0a-
a-b0
X2+
X3-
mX1-
X3-
(a,0)
(a,a)
P
M
M'
AP
Γ5-
mΓ5+
mΓ5+ + mM5+
M2+
A2₁am (A2₁'am')
P4₂/mnm (Pnn'm')
b
T_N
FC
ZFC
M/H (emu/mol)
Γ5- distortion (a.u.)
Polar a-axis (Å)
Temperature (K)
c
Energy (meV/Mn)
Time (arbitrary unit)
P4₂/mnm
Pnma
90º twin
d
Amplitude (Å)
Γ5-
X2+
X3-
Cmc2₁
Pmn2₁
P4₂/mnm
Switching Path

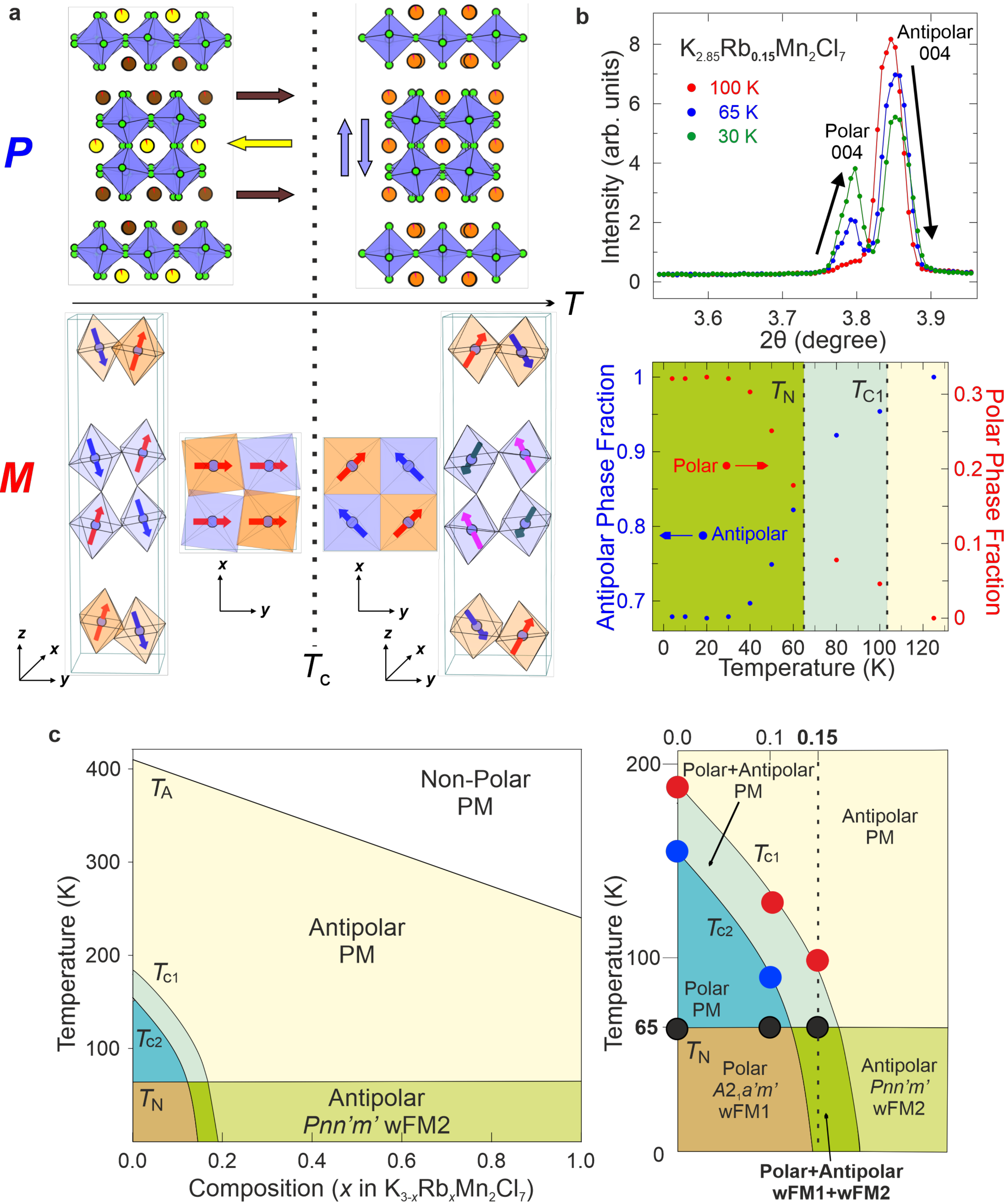
a
P
M
T
T_C
x
y
z
b
K2.85Rb0.15Mn2Cl7
100 K
65 K
30 K
Antipolar
004
Polar
004
Intensity (arb. units)
2θ (degree)
T_N
T_C1
Polar
Antipolar
Antipolar Phase Fraction
Polar Phase Fraction
Temperature (K)
c
T_A
Non-Polar
PM
Antipolar
PM
T_C1
T_C2
T_N
Antipolar
Pnn'm' wFM2
Temperature (K)
Composition (x in K3-xRbxMn2Cl7)
0.0
0.1
0.15
Polar+Antipolar
PM
Antipolar
PM
Polar
PM
Polar
A2₁a'm'
wFM1
Antipolar
Pnn'm'
wFM2
65
Polar+Antipolar
wFM1+wFM2